Article:
Wen, X and Mobbs, S (2014) Numerical simulations of laminar air-water flow of a non-linear progressive wave at low wind speed. Boundary-Layer Meteorology, 150 (3). 381 - 398. ISSN 0006-8314

https://doi.org/10.1007/s10546-013-9876-0

Boundary-Layer Meteorol (2014) 150:381–398
DOI 10.1007/s10546-013-9876-0

RESEARCH ARTICLE

Numerical Simulations of Laminar Air–Water Flow of a Non-linear Progressive Wave at Low Wind Speed

X. Wen · S. Mobbs

Received: 3 January 2013 / Accepted: 22 October 2013 / Published online: 14 November 2013

Abstract A numerical simulation for two-dimensional laminar air–water flow of a non-linear progressive water wave with large steepness is performed when the background wind speed varies from zero to the wave phase speed. It is revealed that in the water the difference between the analytical solution of potential flow and numerical solution of viscous flow is very small, indicating that both solutions of the potential flow and viscous flow describe the water wave very accurately. In the air the solutions of potential and viscous flows are very different due to the effects of viscosity. The velocity distribution in the airflow is strongly influenced by the background wind speed and it is found that three wind speeds, $U = 0$, $U = u_m$ (the maximum orbital velocity of a water wave), and $U = c$ (the wave phase speed), are important in distinguishing different features of the flow patterns.

Keywords Air–water interface · Low wind speed · Progressive wave

1 Introduction

The study of air–water flow is important for the coupling processes between waves and the adjacent airflow. This process is a main research topic for the marine atmospheric boundary layer and ocean boundary layer; a recent review can be found in Sullivan and McWilliams (2010). The air–water flow has received considerable attention over time. The first theoretical analysis was the analytical solution for two-layer potential flow and has been well documented in Lamb (1916) and Milne-Thomson (1994).

X. Wen (✉)
Institute for Climate and Atmospheric Science, School of Earth and Environment,
Centre for Computational Fluid Dynamics, University of Leeds, Leeds LS2 9JT, UK
e-mail: x.wen@leeds.ac.uk

S. Mobbs
National Centre for Atmospheric Science, Centre for Computational Fluid Dynamics, University of Leeds,
Leeds LS2 9JT, UK
e-mail: s.d.mobbs@leeds.ac.uk

Laboratory and field studies on ocean surface waves have been carried out in many previous studies. Kawai (1982) measured velocity distributions in the air using the suspended particle technique, and Mitsuyasu and Honda (1982) measured the growth of the water waves. Cheung and Street (1988) measured the turbulent velocity distribution in the water under an air–water interface, while Hasselmann and Bosenberg (1991) measured the pressure in the air at two-fixed points above the mean water level and analyzed the growth and decay of the interface. Banner and Peirson (1998), using particle image velocimetry (PIV) techniques, measured the velocity distributions beneath wind-driven air–water interfaces and analyzed the tangential stress. Donelan (1999) conducted a laboratory experiment to determine the wave growth and attenuation in following and opposing airflow. More recently, Veron et al. (2007) used PIV to measure the velocity distributions in the air and calculated the shear stress. Peirson and Garcia (2008) measured the wind-induced growth of slow water waves. The coupled boundary layer air–sea transfer field campaigns of Black et al. (2007), Chen et al. (2007) and Edson et al. (2007) are the most recent observations and measurements of air–sea flow.

The field observations and experimental measurements have revealed many valuable and important details of the characteristics of wind-waves such as the movement of the water surface, the distributions of the velocity, shear stress and pressure above the wave crest. However, the movement of the water surface has caused formidable difficulties in the measurements, which can only be made well above the peak of the wave; and hence, many details of the water and airflow in the vicinity of the surface have not been revealed. In fact, there is still a lack of detailed measurements of the velocity in the water and air near the surface. It is also still difficult to find detailed measurements of pressure and shear-stress distributions in both water and air near the interface.

The wave generation theories of Miles (1957) and Phillips (1957) are popular and influential theoretical models of air–sea flow. The theoretical model based on perturbation solutions of the airflow equations is developed by Belcher and Hunt (1998), and this model has revealed many important features of the airflow over a wavy surface. Ocean wave forecasting models have been developed since 1970 (Janssen 2008) and have been widely used in practical applications. These models have a unique attractive feature because of their energy balance equations, but there are uncertainties in the empirical calculations of the energy input, wave–wave interaction and energy dissipation since the mechanism of the interaction between the water wave and the airflow is still not fully understood.

Recent studies have begun to apply computational fluid dynamics (CFD) methods to reveal the details of ocean surface waves. Numerical simulations have been performed for potential flow based on boundary integral methods. Tsai and Yue (1996) reviewed and summarized studies in this research area. Later, numerical simulations of viscous airflow over a stationary wavy boundary were performed by De Angelis et al. (1997) and Henn and Sykes (1999). However, the airflow over a travelling wave is different from that over a stationary wavy boundary. Numerical studies have also been performed for the more realistic airflow above a travelling wavy surface by Al-Zanaidi and Hui (1984) who simulated the turbulent flow over a small Stokes wave using a two-equation turbulence model. Maat and Makin (1992) investigated the effects of the wave steepness on the flow pattern in the air above the Stokes wave by employing a turbulent model. Meirink and Makin (2000) used a low Reynolds number model to simulate the airflow above a sinusoidal wave. In reality the water surface has flatter troughs and sharper crests. In order to simulate these more realistic water waves, Li et al. (2000) studied the turbulent airflow above the Stokes wave using low- and higher-order turbulence models. Sullivan et al. (2000) and, more recently, Yang and Shen (2010) simulated the turbulent airflow above a sinusoidal wave using direct numerical simulation

(DNS). Sullivan et al. (2008) employed a large-eddy simulation (LES) model to analyze situations with airflow following and opposing fast–propagating sinusoidal waves.

These CFD models have developed significantly in the last three decades from early potential flow to later, more complex, turbulent models and DNS. The CFD simulations have substantially increased our knowledge on air–water flow, especially the airflow in the vicinity of the water surface. In these numerical simulations the shape and movement of the wave surface are described by the analytical solution of the Laplace equation for potential flow.

In order to reveal how the airflow affects the water wave, McWilliams et al. (1997), Tsai et al. (2005) and Sullivan et al. (2007) numerically simulated turbulent shear flow in water driven by the surface stress exerted on the flat water surface.

It has long been a desire that the numerical solution for air–water flows should be obtained by including both air and water in a fully coupled formulation, i.e. the two-phase flow model that simultaneously computes the movement of the wave surface and distributions of velocity and pressure in the water and air. It is rare that the Navier–Stokes equations are solved for the two phase air–water flows. Only recently have numerical simulations been performed utilizing a two-phase model.

There are two types of two-phase models: the first solves the Navier–Stokes equations in the domains separately occupied by the air and water and then the solutions for the air and water are coupled by the conditions of continuous velocity and shear stress at the interface. Lin et al. (2008) used this method to investigate the generation of water waves in a turbulent airflow. The effects of the waves on the turbulence above and below the interface are examined, and the numerically predicted wavelength of the fastest growing wave agrees with laboratory measurement. The numerical wave growth rate is consistent with previous studies but may be several times larger. Similarly, Yang and Shen (2011) coupled the solutions in air and water by using the conditions at the interface to simulate laminar and turbulent interfacial flows of a linear progressive wave, and their numerical results agree very well with the analytical solutions.

A second type of two-phase model solves the Navier–Stokes equations in the whole solution domain in order to produce solutions in the air and water simultaneously. Fulgosi et al. (2003) used this approach for the capillary water waves generated by airflow. A two-dimensional, viscous, laminar, progressive water wave has been studied by Raval et al. (2009) when the wind speed is zero by utilizing a coupled two-phase model based on a collocation grid system. Some characteristics of the water wave have been revealed but they did not present the numerical solutions in the air. When the wind speed is zero, a laminar air–water flow of a progressive wave was computed using the recently developed Wet/Dry Areas Method (Wen 2013).

Low wind speed is the condition under which the airflow speed is lower than the wave phase speed. Under such conditions, the features of the air–water flow are significantly different from those with a higher wind-speed. Low wind-speed cases have been studied by Smedman et al. (1999), Grachev and Fairall (2001) and Edson et al. (2007) in their field observations. Hanley and Belcher (2008) analyzed the wave-driven wind jets using a theoretical model. Sullivan et al. (2008) examined the interaction between atmospheric turbulence and swell using a LES model. All these studies reported an upward momentum transfer from the ocean to the atmosphere under low wind-speed conditions.

The laminar flow of the air–water wave is a regime of viscous fluid flow and the behaviour of laminar flow at low wind speeds has a direct connection to the wave generation, flow separation, growth and attenuation. The aim of our study is to investigate the effect of wind speed on the air–water flow pattern as a non-linear progressive wave propagates along the interface between the air and water. Section 2 describes the numerical method and the simu-

lation parameters used in the calculations. Section 3 compares the profiles of the interface of the numerical solution with the analytical solution when the wind speed is zero, and Sect. 4 investigates the effect of wind on the velocity and streamlines. Section 5 compares the horizontal velocities of the viscous and potential flows along the vertical lines passing through the peak and trough of the wave and the average horizontal velocity. Finally, Sect. 6 draws conclusions.

2 Problem Formulation

2.1 Numerical Method

Shown in Fig. 1 is a two-dimensional incompressible air and water flow, where the flow above a progressive water wave has an average wind speed U and exits the solution domain from the outlet at the far right. Water waves with zero current velocity are continuously generated at the inlet at the left end of the domain and propagate in the positive x direction and dissipate on a step shape beach with an average slope of 1/20 at the far right end of the domain. The elevation of the progressive wave is η with the wave amplitude a. The wavelength is L, periodic time is T, wavenumber $k = 2\pi/L$, angular frequency $\sigma = 2\pi/T$, wave phase speed $c = L/T = \sigma/k$, wave steepness $2a/L$, the depth of water is h and the depth of air is h'. $\mathbf{v} = u\mathbf{i} + w\mathbf{j}$ is the velocity vector, p is the pressure, ρ is the density of the fluids, μ is the viscosity of the fluids; here ρ refers to the water density ρ_{w} in the water and the air density ρ_{a} in the air; μ refers to the water viscosity μ_{w} in the water and the air viscosity μ_{a} in the air, g is acceleration due to gravity. The Reynolds number is defined by $Re = \rho_{\mathrm{a}} UL/\mu_{\mathrm{a}}$. The frame of reference is a Cartesian coordinate system (x, z) fixed on the ground and is aligned to the mean water surface shown in Fig. 1.

Let Ω be a control volume in the fluid and we use the Navier-Stokes equations in conservative integral form Hirsch (1997) for the numerical simulation. When the length in the y direction is unity, a two-dimensional flow can be modelled by the three-dimensional Navier–Stokes equations by assuming $\Delta y = 1$ and $v = 0$. For a three-dimensional control volume, $\Omega = \Delta x \times 1 \times \Delta z = \Delta x \times \Delta z$, the continuity equation for volume conservation is written as

$$\int_{\mathrm{S}} (\mathbf{n} \cdot \mathbf{v}) \mathrm{d}S = 0 \tag{1}$$

where $\mathbf{n} = n_x\mathbf{i} + n_z\mathbf{j}$ is a dimensionless unit vector outward from the surface of the control volume S. The continuity equation for mass conservation is written as

$$\int_{\Omega} \frac{\partial \rho}{\partial t} \, \mathrm{d}\Omega + \int_{\mathrm{S}} (\rho \mathbf{n} \cdot \mathbf{v}) \, \mathrm{d}S = 0. \tag{2}$$

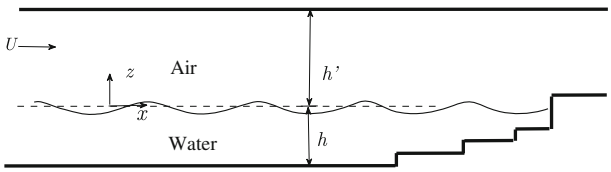

Fig. 1 Sketch of computational domain

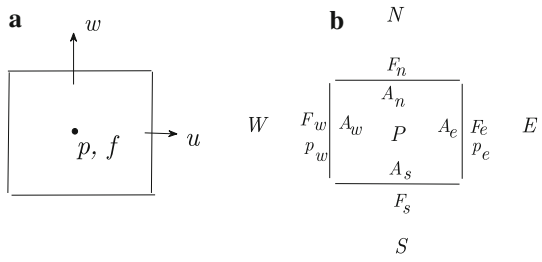

Fig. 2 **a** Staggered location for u, w, p and f; **b** u control volume

The momentum equation for u is given by

$$\int_{\Omega} \frac{\partial(\rho u)}{\partial t}\,\mathrm{d}\Omega + \int_{\mathrm{S}} (\rho \mathbf{n}\cdot\mathbf{v})u\,\mathrm{d}S = -\int_{\mathrm{S}} n_x p\,\mathrm{d}S + \int_{\mathrm{S}} \mu\frac{\partial u}{\partial l}\,\mathrm{d}S \tag{3}$$

and the momentum equation for w is given by

$$\int_{\Omega} \frac{\partial(\rho w)}{\partial t}\,\mathrm{d}\Omega + \int_{\mathrm{S}} (\rho \mathbf{n}\cdot\mathbf{v})w\,\mathrm{d}S = -\int_{\mathrm{S}} n_z p\,\mathrm{d}S + \int_{\mathrm{S}} \mu\frac{\partial w}{\partial l}\,\mathrm{d}S - mg \tag{4}$$

where $m = \int_{\Omega} \rho\,\mathrm{d}\Omega$ is the total fluid mass within the control volume, $\frac{\partial}{\partial l}$ is the directional derivative along the direction of $\mathbf{n}$. Here f is the fractional volume of Ω occupied by the water and satisfies

$$\int_{\Omega} \frac{\partial f}{\partial t}\,\mathrm{d}\Omega + \int_{\mathrm{S}} (\mathbf{n}\cdot\mathbf{v})f\,\mathrm{d}S = 0. \tag{5}$$

The staggered grid arrangement for u, w, p and f is shown in Fig. 2a; the control volume for the velocity component u is shown in Fig. 2b. By applying the standard control volume method described by Patankar (1980) and Shyy (1994) we obtain the following standard algebraic equations for u and w:

$$\begin{aligned} a_P u_P = {} & a_E u_E + a_W u_W + a_N u_N + a_S u_S \\ & + p_w A_w - p_e A_e + \frac{m_0}{\Delta t}(u_P)_0 + u_b, \end{aligned} \tag{6}$$

$$\begin{aligned} a_P w_P = {} & a_E w_E + a_W w_W + a_N w_N + a_S w_S \\ & + p_s A_s - p_n A_n + \frac{m_0}{\Delta t}(w_P)_0 - mg + w_b. \end{aligned} \tag{7}$$

The coefficients are given by

$$\left.\begin{aligned} & a_E = D_e + [-F_e, 0], \qquad a_W = D_w + [F_w, 0], \\ & a_N = D_n + [-F_n, 0], \qquad a_S = D_s + [F_s, 0], \\ & D_e = (\mu\frac{A}{\Delta x})_e, \qquad D_w = (\mu\frac{A}{\Delta x})_w, \\ & D_n = (\mu\frac{A}{\Delta z})_n, \qquad D_s = (\mu\frac{A}{\Delta z})_s, \\ & a_P = \frac{m_0}{\Delta t} + a_E + a_W + a_N + a_S = \frac{m_0}{\Delta t} + \Sigma a_{nb} \end{aligned}\right\} \tag{8}$$

where subscript 0 represents the solution at time level n and other symbols represent the solution at time level $n+1$. $[a, b]$ represents the maximum of the two operands a and b. Terms u_b and w_b contain the contributions from the higher-order terms.

F_e, F_w, F_n and F_s are the fluid fluxes passing through surfaces A_e, A_w, A_n and A_s at time level $n+1$ and are given by

$$\left.\begin{aligned} F_e &= \int_{A_e} \rho u \, \mathrm{d}S, \qquad F_w = \int_{A_w} \rho u \, \mathrm{d}S \\ F_n &= \int_{A_n} \rho w \, \mathrm{d}S, \qquad F_s = \int_{A_s} \rho w \, \mathrm{d}S. \end{aligned}\right\} \tag{9}$$

These mass fluxes are calculated by the Wet/Dry Areas Method (Wen 2013). For the volume fraction f, a high resolution scheme compressive interface capturing scheme for arbitrary meshes developed by Ubbink and Issa (1999) for the volume of fluid method is used to solve Eq. 5 in order to track the interface.

The feature of the Wet/Dry Areas Method used herein is that the mass fluxes passing through the surfaces of the control volume are calculated by an algebraic expression derived from the conservative integral form of the Navier–Stokes equations. Wen (2012) explained why this method produces numerical solution with high accuracy.

2.2 Initial and Boundary Conditions

Since there is no analytical solution of the Navier–Stokes equations available for us to specify the initial and boundary conditions, the best possible approximation for the problem is the analytical solution of potential flow. In the solution of a linear progressive wave in a two-layer potential flow (Milne-Thomson 1994), the surface elevation, η, of the wave travelling in the x-direction is

$$\eta = a \ \sin(kx - \sigma t). \tag{10}$$

The velocity components, pressure and volume fraction in the air are given by

$$u = U - B_\mathrm{a} akc \sin(kx - \sigma t) \cosh k(z - h'), \tag{11}$$

$$w = B_\mathrm{a} akc \cos(kx - \sigma t) \sinh k(z - h'), \tag{12}$$

$$p = -\rho_\mathrm{a} akc^2 B_\mathrm{a} \cosh k(z - h') \sin(kx - \sigma t) - \rho \tfrac{u^2+w^2}{2} - \rho g z, \tag{13}$$

$$f = 0. \tag{14}$$

In the water they are given by

$$u = B_\mathrm{w} akc \sin(kx - \sigma t) \cosh k(z + h), \tag{15}$$

$$w = -B_\mathrm{w} akc \cos(kx - \sigma t) \sinh k(z + h), \tag{16}$$

$$p = \rho_\mathrm{w} akc^2 B_\mathrm{w} \cosh k(z + h) \sin(kx - \sigma t) - \rho_\mathrm{w} \tfrac{u^2+w^2}{2} - \rho_\mathrm{w} g z, \tag{17}$$

$$f = 1, \tag{18}$$

where

$$B_\mathrm{a} = \frac{(1 - U/c)}{\sinh kh'}, \tag{19}$$

and

$$B_\mathrm{w} = \frac{1}{\sinh kh}. \tag{20}$$

The dispersion equation takes the following form

$$\rho_{\mathrm{w}}\sigma^2 \coth kh + \rho_{\mathrm{a}}(\sigma - kU)^2 \coth kh' = (\rho_{\mathrm{w}} - \rho_{\mathrm{a}})gk, \tag{21}$$

or

$$\rho_w c^2 \coth kh + \rho_a (c - U)^2 \coth kh' = \frac{(\rho_w - \rho_a)g}{k}. \tag{22}$$

The initial surface elevation of the water wave and velocity distributions in the air and water are evaluated by substituting $t = 0$ into Eqs. 10–21. When $t > 0$, the location of the interface and the velocity of the water and air at the inlet are calculated by substituting $x = 0$ into (10)–(12), (14)–(16) and (18). At the top of the domain, a symmetric condition for the velocity is applied. At the bottom and on the step beach, a no-slip wall condition is applied. At the outlet, the normal derivative of velocity is set to zero.

2.3 Simulation Parameters

In the numerical simulation, the water and air depth was set to $h = 0.12$ m and $h' = 0.78$ m, respectively. The wavelength for the water wave is set to $L = 0.2$ m and wave amplitude to $a = 0.008$ m, which leads to a deep water wave with $h/L = 0.6$ and a large wave steepness $2a/L = 0.08$ ($ak = 0.2513$). The wave phase speed, c, is calculated using Eq. 22. In order to find the effect of the wind, the numerical simulations are performed at $U = 0$, u_{m}, $0.5c$ and c, respectively, where u_{m} is the maximum water orbital velocity at the peak of the wave of the potential flow and is obtained by setting $t = 0$, $kx - \sigma t = \pi/2$ and $z = a$ in Eq. 15,

$$u_{\mathrm{m}} = B_{\mathrm{w}} akc \cosh k(a + h). \tag{23}$$

As sketched in Fig. 1, the length of the computational domain is 4 m and the length of the main test domain is 3 m which accommodates 15 wavelengths. The length of step shape beach is 0.65 m with an average slope of 1/20. At the end of the beach is a vertical wall jointed by a horizontal outlet channel with a width of 0.63 m. The values of the parameters used in the simulation are $g = 9.8$ m s^{-2}, water viscosity $\mu_{\mathrm{w}} = 1.0 \times 10^{-3}$ kg m^{-1} s^{-1}, air viscosity $\mu_{\mathrm{a}} = 1.0 \times 10^{-5}$ kg m^{-1} s^{-1}, $\rho_{\mathrm{w}} = 1000$ kg m^{-3} and $\rho_{\mathrm{a}} = 1.0$ kg m^{-3}. The Reynolds number varies from 0 to 11,152.

A rectangular non-uniform Cartesian mesh is used in the whole solution domain. In order to resolve the boundary layer at the bed, $\Delta z = 0.0001$, 0.0003 and 0.0005 m were tested for the first grid size. It is found that $\Delta z = 0.0001$ and 0.0003 m produce accurate solutions, so $\Delta z = 0.0003$ m is used. Above the first grid, the grid size increases to the middle of the water wave where the grid size starts to decrease. Uniform grids with 8, 12, 16 and 20 grid points were tested to cover the wave height. It was found that both 12 and 16 grid points are sufficient to produce accurate results, therefore, 16 grid points are distributed vertically around the wave height. Above the peak of the wave, the grid size gradually increases to the top of the domain. A total of 60, 90 and 120 grid points in z direction were tested, and 90 grid points was found to be sufficient to produce accurate results.

In the horizontal direction, a uniform mesh is used with the grid size of $\Delta x = 3\Delta z_{\mathrm{wave}}$, where Δz_{wave} is the grid size at the wave height. The time of numerical simulations lasts until the wave generated at the inlet at $t = 0$ propagates to the middle of the beach. The timestep varies from 0.00005 to 0.00002 s as the wind speed varies from $U = 0$ to $U = c$.

In order to further dissipate the energy on the beach at the right end of the solution domain an artificial viscosity is added to the air and water on the beach. We use the following equation to generate the artificial viscosity

$$\mu_T = (A\Delta)^2 \rho \sqrt{2 S_{ij} S_{ij}} \tag{24}$$

where $S_{i,j} = \frac{1}{2}(\frac{\partial u_i}{\partial x_j} + \frac{\partial u_j}{\partial x_i})$, Δ is the grid size and A is an arbitrary constant. In the calculation we chose $A = 10-100$, which produces a nearly flat water surface at the right end of the beach. When this artificial viscosity was added, the length of the beach and the computational cost were substantially reduced.

3 The Comparison of the Profiles of the Numerical and Analytical Solutions When $U = 0$

For viscous flow, Fig. 3 shows the numerically predicted profile of the interface of the first five waves when the wind speed is zero. It is observed that the interface of the numerical solution is periodic. The most remarkable feature of the numerical solution is that the interface has flatter troughs and sharper crests.

When the wind speed is zero, it is also interesting to compare the numerically produced profile of the water surface with profiles produced by the solution of the linear wave given by (10) and the fifth-order solution of the nonlinear wave of Fenton (1985) given by

$$\begin{aligned}\eta = {} & a\cos(kx-\sigma t) + \frac{1}{2}kh^2\cos\left[2(kx-\sigma t)\right] + \frac{3}{8}k^2h^3\Big\{\cos\left[3(kx-\sigma t)\right] \\ & -\cos(kx-\sigma t)\Big\} + \frac{1}{3}k^3h^4\Big\{\cos\left[2(kx-\sigma t)\right] + \cos\left[4(kx-\sigma t)\right]\Big\} \\ & + \frac{1}{384}k^4h^5\Big\{-422\cos\left[(kx-\sigma t)\right] + 297\cos\left[3(kx-\sigma t)\right] \\ & + 125\cos\left[5(kx-\sigma t)\right]\Big\}. \end{aligned} \tag{25}$$

Starting at a location of two wavelengths from the inlet, Fig. 4 presents the profiles of the wave surface produced by (10), (25) and the numerical solution. Figure 4 shows an excellent agreement between the numerical and the fifth-order solutions. The linear wave given by

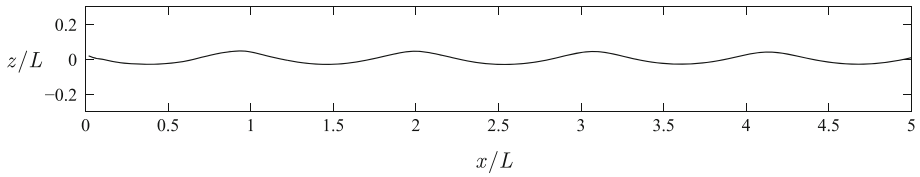

Fig. 3 The interface of the first five waves of the viscous flow when $U = 0$

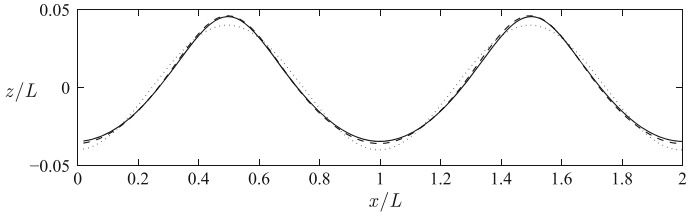

Fig. 4 Comparison of profiles of the wave surface for $U = 0$: *dotted line* linear wave; *spaced dash* Fenton's fifth-order solution; *line* numerical solution

(10) is a sinusoid that has the same profile above and below the mean water surface, whereas the numerical and fifth-order solutions have flatter troughs and sharper crests than the linear wave.

Another notable difference between the linear wave and Fenton's fifth-order and numerical solutions is that the fifth-order and numerical solutions have higher elevation at the peak and trough. The profile of the input wave at the inlet is the linear wave given by (10), thus Fig. 4 reveals that the linear wave input at the inlet quickly evolves to the non-linear viscous wave once it propagates into the solution domain. The excellent agreement between the fifth-order and numerical solutions indicates that both Fenton's theoretical relation and the numerical solution produce accurate profiles for the wave surface when the wind speed is zero.

4 Velocity Vectors and Streamlines

From this section we present the results for the fifth wave from the inlet since the difference between the waves are small. We use velocity vectors and streamlines to present the velocity distribution and the flow pattern locally and also globally. The dimensionless velocity is defined as

$$\bar{u} = \frac{u}{akc}, \tag{26}$$

$$\bar{w} = \frac{w}{akc}, \tag{27}$$

and the dimensionless streamfunction is defined as

$$\bar{\psi} = \frac{\psi}{ac}. \tag{28}$$

For the different wind speeds $U = 0, u_{\mathrm{m}}, 0.5c$ and c, Figs. 5 and 6 plot the velocity vectors and streamlines of the fifth wave produced by the numerical solutions of viscous flow and the analytical solutions of potential flow given by (10)–(21). Figures 7 and 8 present the detailed velocity distributions of the fifth wave of the viscous flow. In general, Figs. 5 and 6 show the viscous and potential flows have very similar flow patterns. The velocity vectors and streamlines of the viscous and potential flows are almost the same in the water and in most of the air. The airflow changes significantly with the wind speed in both viscous and potential flows. The notable difference between the viscous and the potential flows is that the velocity of the viscous flow is a continuous function in the solution domain including at the interface, whereas the velocity of the potential flow is discontinuous at the interface because the viscosity is ignored in the potential flow.

Figures 5a, b, and 6a, b show the results of the viscous and potential flows when the wind speed $U = 0$. The viscous flow in Figs. 5a and 6a exhibits two rotating flows centred in the air, one anti-clockwise rotating flow just above the peak of the water wave and one clockwise rotating flow just above the trough. They both roll forward with the wave phase speed c due to the propagation of the crest and trough. From Figs. 5a and 6a we can see that the two rotating flows in the air are induced by the orbital motion of the water wave. Figures 7a and 8a show the detailed velocity distributions of the viscous flow at the crest and trough in Fig. 5a. The analytical solutions of potential flow in Figs. 5b and 6b are simply two sinusoidal waves, one in the water described by (15) and (16) and the other in the air described by (10) and (11).

Figures 5c and 6c show the instantaneous velocity vectors and streamlines of the viscous flow when the wind speed is increased to the maximum wave orbital velocity $U = u_{\mathrm{m}} =$

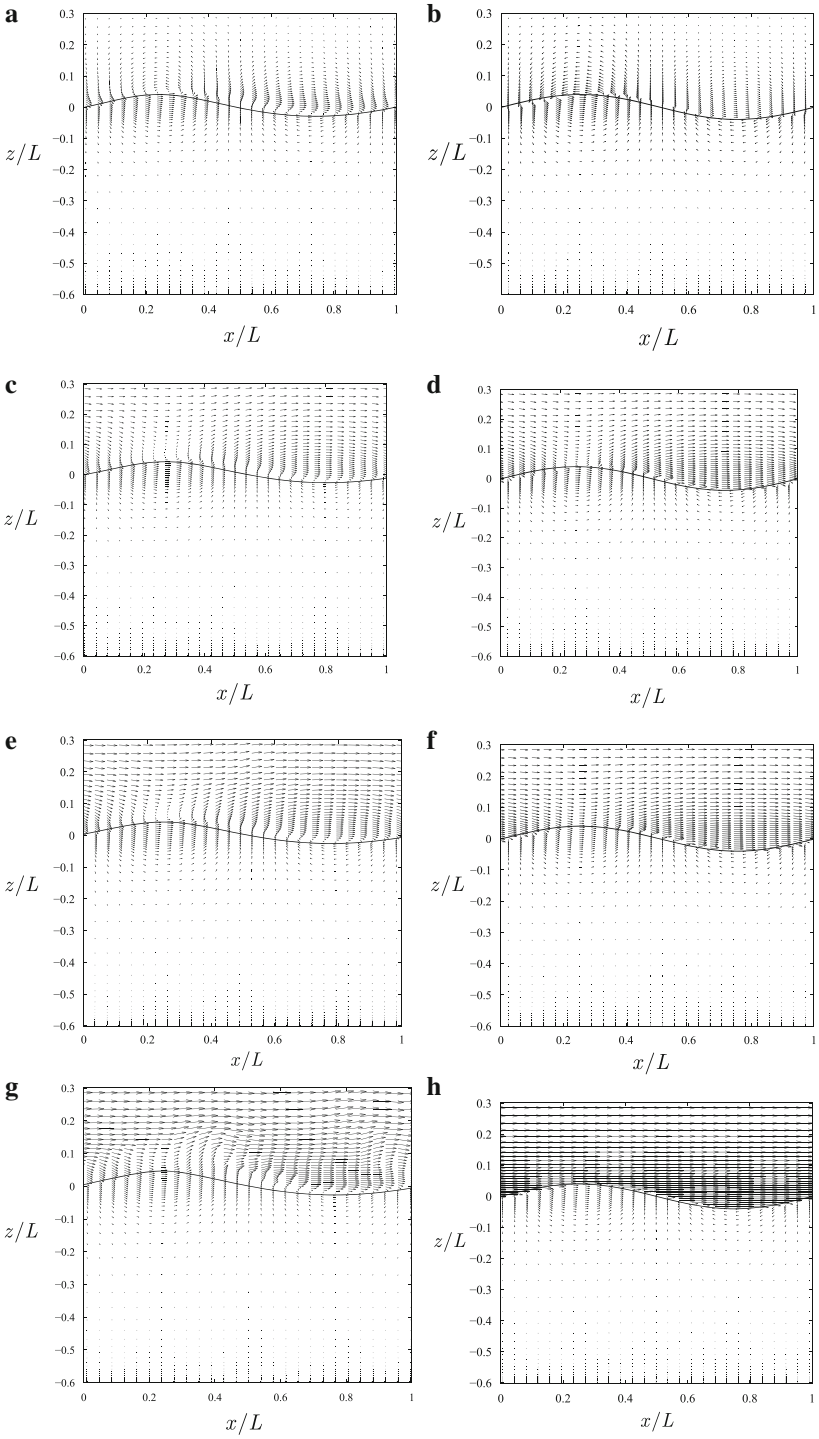

Fig. 5 Velocity vectors of viscous flow on the *left* in panels (**a**, **c**, **e**, **g**) and potential flow on the *right* in panels (**b**, **d**, **f**, **h**) when $U = 0, u_m, 0.5c$ and c (from top to bottom), respectively

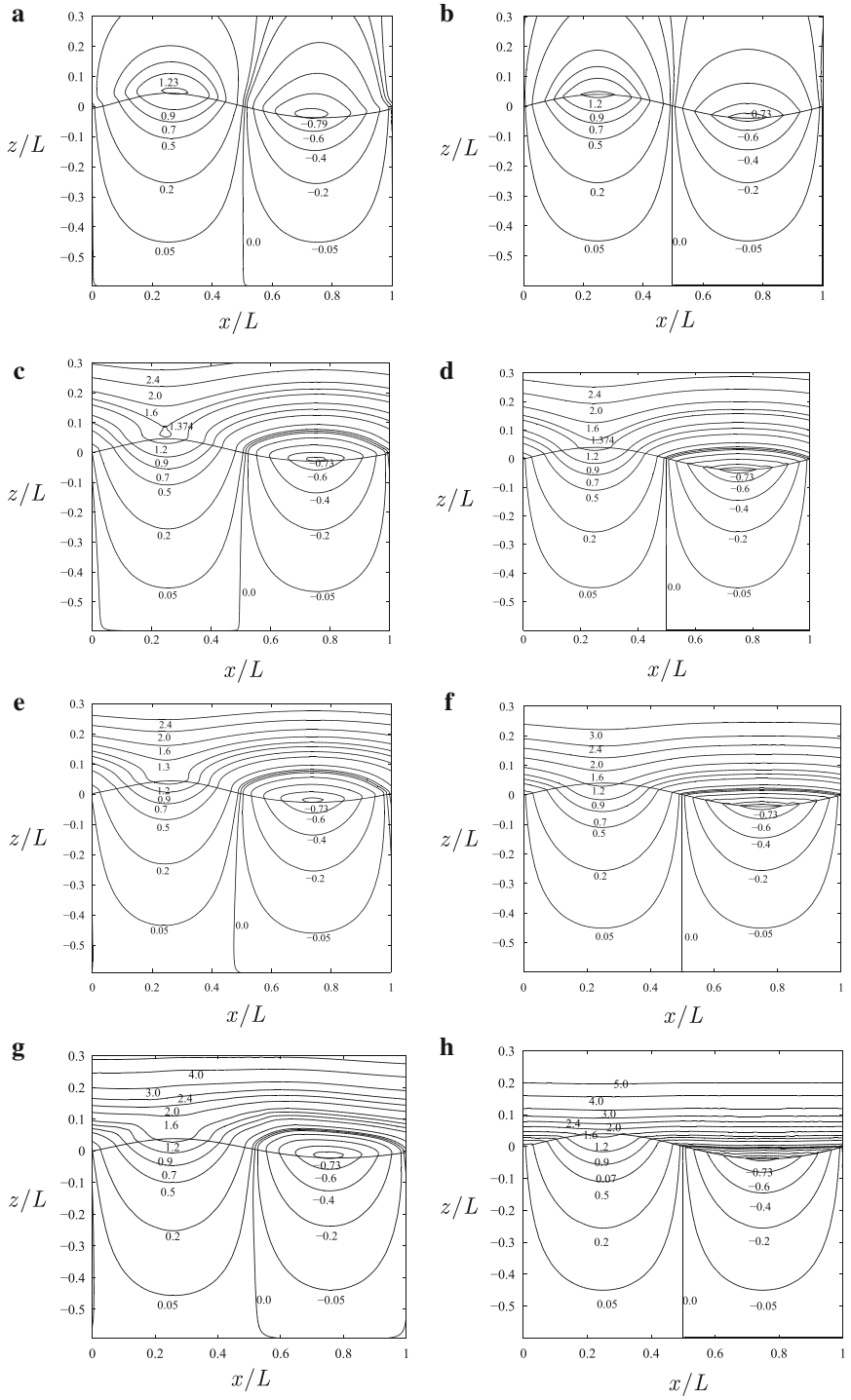

Fig. 6 Streamlines of viscous flow on the *left* in panels (**a**, **c**, **e**, **g**) and potential flow on the *right* in panels (**b**, **d**, **f**, **h**) when $U = 0, u_{\mathrm{m}}, 0.5c$ and c (from top to bottom), respectively

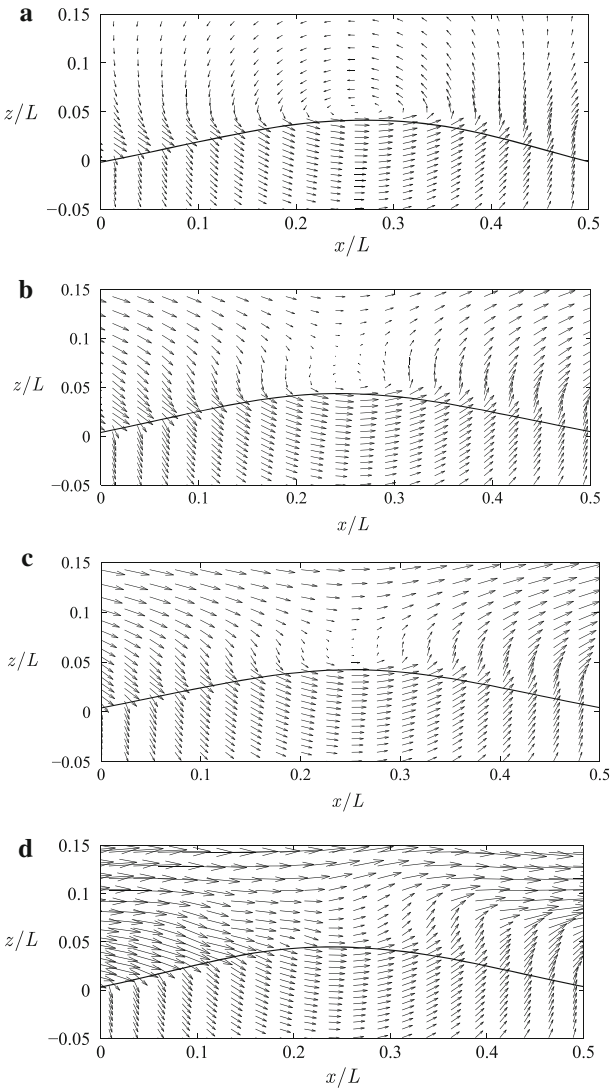

Fig. 7 Detailed velocity distributions of viscous flow at the crest: **a** $U = 0$; **b** $U = u_{\mathrm{m}}$; **c** $U = 0.5c$; **d** $U = c$

$0.323c$. These figures show that most air moves in the wind direction but a tiny rotating flow just above the crest is still visible, indicating that the water orbital motion, which induces the anti-clockwise rotating flow, causes the air above the crest to decelerate. Above the trough, the backward moving water and forward moving air create a rotating flow in the air. Figure 7b reveals the detailed velocity vectors in the small rotating flow above the crest while Fig. 8b shows the detailed velocity distribution in the rotating flow at the trough. The potential flow in Figs. 5d and 6d shows that, unlike the viscous flow, all the air moves with positive velocity along the wind direction.

When the wind speed increases to half of the wave speed ($U = 0.5c$), Figs. 5e and 6e show that, in the numerical results of the viscous flow, the rotating flow above the crest has

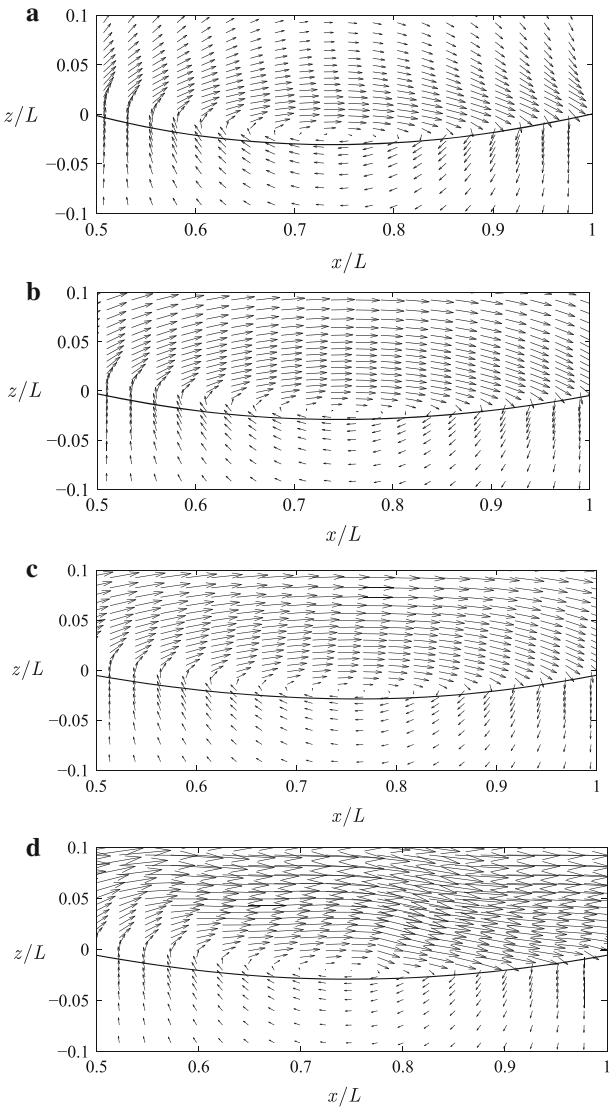

Fig. 8 Detailed velocity distributions of viscous flow at the trough: **a** $U = 0$; **b** $U = u_{\mathrm{m}}$; **c** $U = 0.5c$; **d** $U = c$

completely disappeared and all the air moves forward, but the rotating flow above the trough persists. Figure 7c reveals the very small air velocity of the viscous flow above the crest caused by the wind and water orbital motions. Figure 8c shows that the rotating flow above the trough is very similar to Fig. 8b because of a small increase of the wind speed from $U = u_{\mathrm{m}} = 0.323c$ to $U = 0.5c$. This small increase also causes a small increase in the velocity of the potential flow in the air in Figs. 5f and 6f.

Figures 5g and 6g show the velocity vectors and streamlines of viscous flow when the wind speed is further increased to the wave phase velocity c. It is observed that the air

velocity substantially increases and the streamlines in the main stream of the flow become more horizontal. The top boundary of the rotating flow above the trough is closer to the water surface leading to a smaller rotating flow. Figure 7d reveals that, despite the wind speed being three times the maximum water orbital velocity u_{m}, the air velocity above the peak is still smaller than u_{m}, indicating a very strong effect of the orbiting water on the air. Figure 8d reveals a further decrease in the size of the recirculation above the trough. When $U = c$, (11) and (12) lead to $w = 0$ and $u = c$, therefore, Fig. 5h shows that the potential flow has a constant horizontal velocity everywhere in the air and Fig. 6h shows that all the streamlines in the air are horizontal lines.

5 Horizontal Velocities

In order to further investigate the velocity distributions for the fifth wave, Fig. 9 plots the numerical and analytical horizontal velocities varying with z at two locations $x/L = 0.25$ and $x/L = 0.75$ for different wind speeds. In general, the numerically predicted horizontal velocities are in excellent agreement with the analytical solutions of the potential flow in the water and in most of the air. As revealed in Sect. 4 the differences between the solutions of the viscous and potential flows occur in the air near the water surface.

At the wave crest $x/L = 0.25$, Fig. 9a, c, e, g show that the positive u velocity component of the potential and viscous flows increases monotonically to the maximum from the bed to the water surface. A remarkable feature is that the difference between the velocity magnitudes of the potential and viscous flows is less than 1 %. Across the interface into the air, the velocity u of the viscous flow always decreases even at the wind speed $U = c$. This reduction of the velocity in the air above the crest is clearly caused by the orbital motion of the water. It is observed in Fig. 9a, c, e, d that the reduction becomes smaller with the increase in the wind speed. In Fig. 9g the reduction is almost zero. Therefore, it can be expected that a further increase of the wind speed will not produce a reduction in u and the horizontal velocity u will monotonically increase with z when the wind speed $>$ the wave phase speed.

At the wave trough where $x/L = 0.75$ in Fig. 9b, d, f, h, the negative u velocity component of the potential and viscous flows decreases monotonically to the maximum negative from the bed to the water surface. The viscous flow has a tendency of becoming more positive with the increase in wind speed. Across the interface, the u velocities of both potential and viscous flows increase with z and then decrease again at higher elevations. From the excellent agreement between the analytical and numerical solutions in Fig. 9 we can draw the conclusion that the numerical simulation produces high quality results.

In order to analyse the average characteristics of the air flow above the fifth wave, we define the average of variable ϕ by

$$[\phi](z) = \frac{1}{L}\int_{L} \phi(x, z)\,\mathrm{d}x. \tag{29}$$

Figure 10 represents the profile of the average non-dimensional horizontal velocity $[\bar{u}]$ at different wind speeds. It is observed that when the wind speed is zero the average horizontal velocity is positive near the wave surface and becomes negative at higher elevations due to the circulation flows above the peak and trough, indicating that when the wind speed is small the horizontal velocity does not dominate the flow pattern. In fact, Figs. 5a, 6a, 7a and 8a show the vertical velocity and horizontal velocity have equal magnitude when the wind speed

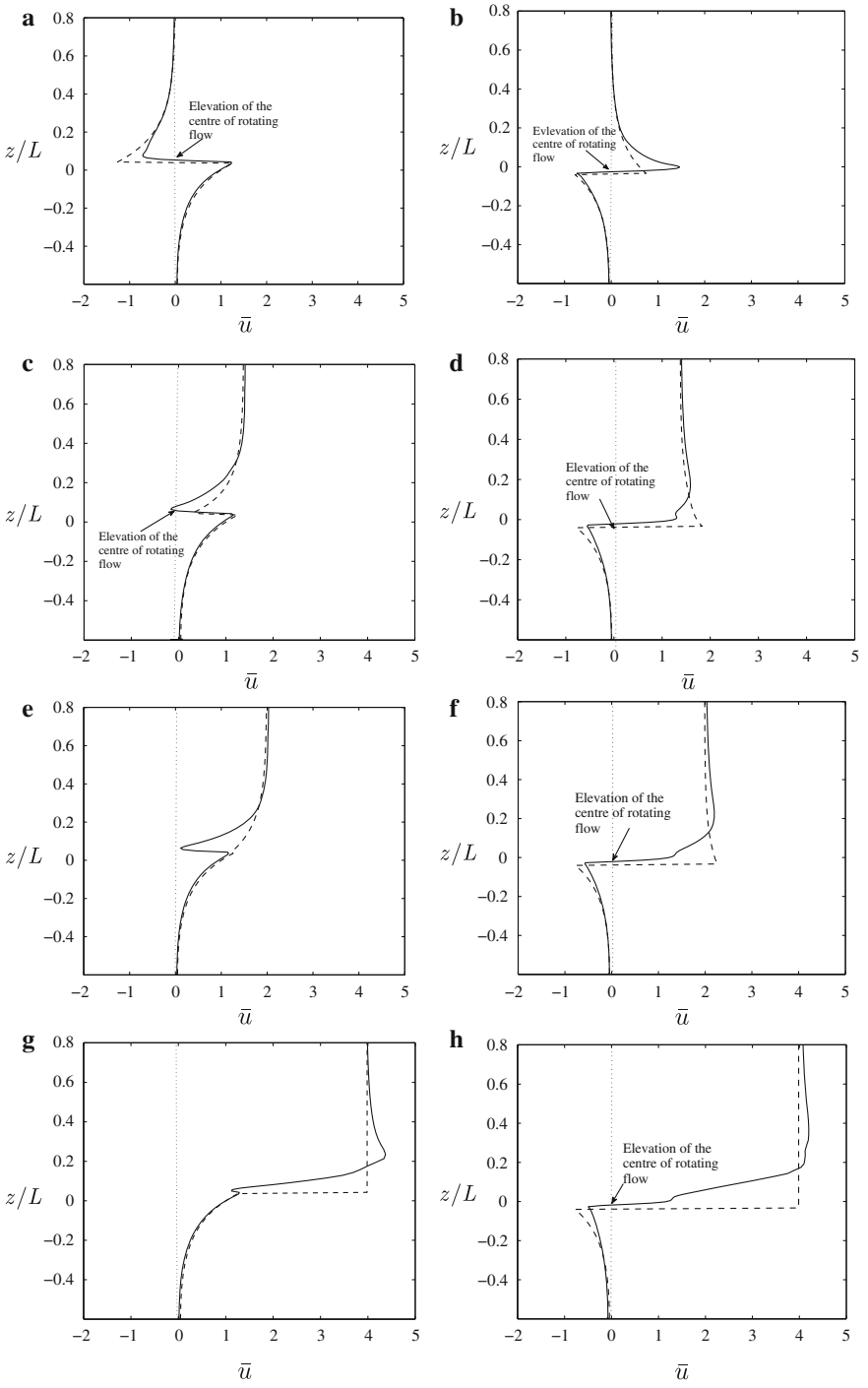

Fig. 9 Variation of horizontal velocity component with z at $x/L = 0.25$ on the *left* in panels (**a**, **c**, **e**, **g**) and $x/L = 0.75$ on the *right* in panels (**b**, **d**, **f**, **h**) when $U = 0$, u_m, $0.5c$ and c (from top to bottom); *line* viscous flow, *spaced dash* potential flow, respectively

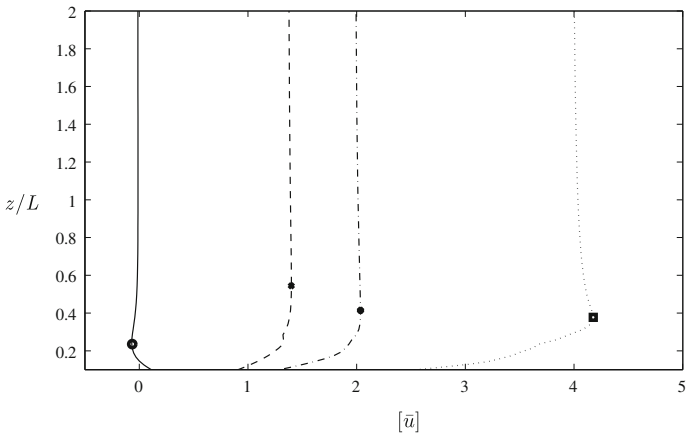

Fig. 10 Average horizontal velocity component normalized by U for different wind speeds: *line* with *circle* $U = 0$, *spaced line* with *star* $U = u_{\mathrm{m}}$, *dotted dash* with *bullet* $U = 0.5c$, *dotted line* with *square* $U = c$

is small. Therefore, it is the vertical velocity that causes the significant upward momentum transfer from the ocean to the atmosphere under low wind-speed conditions.

Figure 10 also shows the average horizontal velocity increases as the wind speed increases. We also observe that the average horizontal velocity increases with z and there is a wind-speed maximum. The marks in Fig. 10 show the wind-speed maximum moves to a lower position when the wind-speed increases, indicating a weakening vertical velocity and increasing horizontal velocity. When the wind speed equals the wave phase speed, Fig. 10 shows that the wind-speed maximum reaches its highest value. Such an increase in the horizontal velocity is very similar to the acceleration of air over the tops of hills or humps shown in Figs. 7d and 9g.

6 Conclusions

In this paper, the effect of low wind speed on air–water flow is investigated when a non-linear progressive wave propagates along the interface between the air and the water. It is shown that, in the water, the velocities of the viscous and potential flows agree extremely well, indicating that the analytical solution of potential flow describes the water wave extremely accurately and the effects of the viscosity on the flow pattern and velocity are very small. In the water, the very small differences between the numerical solutions of viscous fluid and the analytical solutions of potential flow are also an indication that the numerical solutions produced by the Wet/Dry Areas Method (Wen 2013) are highly accurate.

Unlike the water, the airflow near the water surface is strongly influenced by the movement of the water wave, viscosity and wind speed. There is an interesting connection between the flow patterns in the air and water. The airflow has three distinct patterns when the wind speed equals zero, the maximum water orbital velocity u_{m} and the wave phase speed c.

When the wind speed is zero, the domain of air is occupied by two recirculations with opposite rotation. They are formed by wave-induced motions, induced purely by the combination of the orbital movement of the water wave, viscosity and the pressure drop in the vertical direction. The vertical pressure drop is at its largest for zero wind speed, and which causes the strongest upward momentum transport from the water to the air. Therefore, zero wind speed is an important speed for the air–water flow.

When the wind speed is between zero and the maximum wave orbital velocity there exist two circulations in the air—one above the peak and the other above the trough of the water wave. It is interesting to see that when the wind speed is greater than the maximum water orbital velocity, the recirculation and negative horizontal velocity component above the peak of the water wave disappear but the air velocity above the peak is still lower than the maximum wave orbital velocity u_{m}. Therefore, the water maximum orbital wave velocity u_{m} at the peak of the water wave is an important parameter for the air–water flow.

It is also interesting to see that when the wind speed is equal to the wave phase speed c, the air velocity above the peak of the wave increases to the maximum water orbital velocity u_{m}, indicating that the air particle above the peak eventually has the same velocity as the water particle at the peak of the water wave. It is expected that the air velocity at the wave peak will be greater than the water velocity u_{m} at the peak of the wave when the wind speed is greater than the wave phase speed c. Therefore, the wave phase speed is an important parameter for the air–water flow.

We also see that a large and strong rotating flow above the trough of the water wave persists at all different wind speeds due to the large wave slope of the non-linear wave.

Acknowledgments We would like to thank the invaluable comments from the reviewers that significantly improved the previous version of this paper. We also would like to thank the kind help from our colleague Dr. Wuhu Feng at National Centre for Atmospheric Science in the preparation of this paper.

References

Al-Zanaidi MA, Hui WH (1984) Turbulent airflow over water waves—a numerical study. J Fluid Mech 148:225–246

Banner ML, Peirson WL (1998) Tangential stress beneath wind-driven air–water interface. J Fluid Mech 364:115–145

Belcher SE, Hunt JCR (1998) Turbulent shear flow over hills and waves. Ann. Rev. Fluid Mech 30:507–538

Black P, D'Asaro E, Drennan W, French J, Niiler P (2007) Air-sea exchange in hurricanes: synthesis of observations from the coupled boundary layer air–sea transfer experiment. Bull Am Meteorol Soc 88: 357–374

Chen SS, Price JF, Zhao W, Donelan MA, Walsh EJ (2007) The CBLAST-hurricane program and the next-generation fully coupled atmosphere–wave–ocean models for hurricane research and prediction. Bull Am Meteorol Soc 88:311–317

Cheung T, Street RL (1988) Turbulence layers in the water at an air–water interface, part A. J Fluid Mech 194:133–151

Dalrymple RA, Rogers BD (2005) Numerical modeling of water waves with the SPH method. Coast Engine 53:141–147

De Angelis V, Lombardi P, Banerjee S (1997) Direct numerical simulation of turbulent flow over a wavy wall. Phys Fluids 9:2429–2442

Dean RG, Dalrymple RA (1984) Water wave mechanics for engineers and scientists. Prentice-Hall Inc., New Jersey, 353 pp

Donelan MA (1999) Wind-induced growth and attenuation of laboratory waves. In: Sajjadi SG, Thomas NH, Hunt JCR (eds) Wind-over-waves couplings: perspectives and prospects, Clarendon Press, Oxford, 356 pp

Edson J, Crawford T, Crescent J, Farrar T, French J (2007) The coupled boundary layer and air–sea transfer experiment in low winds (CBLAST-Lpw). Bull Am Meteorol Soc 88:342–356

Fenton J (1985) A fifth-order Stokes theory for steady waves. Waterw Port Coast Ocean Eng 111(2):216–234

Fulgosi M, Lakehal D, Banerjee S, Angelis VD (2003) Direct numerical simulation of turbulence in a sheared air–water flow with a deformable interface. J Fluid Mech 482:319–345

Grachev AA, Fairall CW (2001) Upward momentum transfer in the marine boundary layer. J Phys Oceanogr 31:1698–1711

Hanley KE, Belcher SE (2008) Wave-driven wind jets in the marine atmospheric boundary layer. J Phys Oceanogr 65:2646–2660

Hasselmann D, Bosenberg J (1991) Field measurements of wave-induced pressure over wind–sea and swell. J Fluid Mech 230:391–428
Henn DS, Sykes RI (1999) Large-eddy simulation of flow over wavy surface. J Fluid Mech 383:75–112
Hirsch C (1997) Numerical computation of internal and external flows. Wiley, Chichester
Janssen P (2008) Progress in ocean wave forecasting. J Comp Phys 227:3572–3594
Kawai S (1982) Structure of air flow separation over wind wave crests. Boundary-Layer Meteorol 23:503–521
Lamb H (1916) Hydrodynamics. Cambridge University Press, U.K. 708 pp
Li PY, Xu D, Taylor PA (2000) Numerical modelling of turbulent airflow over water waves. Boundary-Layer Meteorol 95:397–425
Lin M, Moeng CH, Tsai W, Sullivan PP, Belcher SE (2008) Direct numerical simulation of wind–wave generation process. J Fluid Mech 616:1–30
Maat N, Makin VK (1992) Numerical simulation of air flow over breaking wave. Boundary-Layer Meteorol 60:77–93
McWilliams JC, Sullivan PP, Moeng CH (1997) Langmuir turbulence in the ocean. J Fluid Mech 334:1–30
Meirink JF, Makin VK (2000) Modelling low Reynolds number effects in the turbulent airflow over water waves. J Fluid Mech 415:155–174
Miles JW (1957) On the generation of surface waves. J Fluid Mech 3:185–204
Milne-Thomson LM (1994) Theoretical hydrodynamics. Dover Publications Inc., NewYork, 743 pp
Mitsuyasu H, Honda T (1982) Wind-induced growth of water waves. J Fluid Mech 123:425–442
Patankar SV (1980) Numerical heat transfer and fluid flow. Hemisphere Publishing Corporation, USA, 197 pp
Peirson WL, Garcia AW (2008) On the wind-induced growth of slow water waves of finite steepness. J Fluid Mech 608:243–274
Peirson WL, Garcia AW, Pells SE (2003) Water wave attenuation due to opposing wind. J Fluid Mech 487: 345–365
Phillips OM (1957) On the generation of waves by turbulent wind. J Fluid Mech 2:417–445
Raval A, Wen X, Smith M (2009) Numerical simulation of viscous, non-linear and progressive water waves. J Fluid Mech 637:443–473
Shyy W (1994) Computational modelling for fluid flow and interfacial transport. Elsevier, Amsterdam, 504 pp
Smedman A, Hogstrom U, Bergstrom H, Rutgersson A, Kahma KK, Pettersson H (1999) A case study of air–sea interaction during swell conditions. Geophys Res Ocean 104(C11):25833–25851
Sullivan PP, McWilliams JC (2010) Dynamics of winds and currents coupled to surface waves. Annu Rev Fluid Mech 42:19–42
Sullivan PP, McWilliams JC, Moeng CH (2000) Simulation of turbulent flow over idealized water waves. J Fluid Mech 404:47–85
Sullivan PP, McWilliams JC, Melville WK (2007) Surface gravity wave effects in the oceanic boundary layer: large-Eddy Simulation with vortex force and stochastic breakers. J Fluid Mech 593:405–452
Sullivan PP, Edson JB, Hristov T, McWilliams JC (2008) Large-Eddy simulations and observations of atmospheric marine boundary layers above nonequilibrium surface waves. Atm Sci 65:1225–1245
Tsai WT, Yue DKP (1996) Computation of nonlinear free-surface flows. Annu Rev Fluid Mech 28:249–278
Tsai WT, Chen SM, Moeng CH (2005) A numerical study on the evolution and structure of a stress-driven free-surface turbulent shear flow. J Fluid Mech 545:163–192
Ubbink O, Issa RT (1999) Method for capture sharp fluid interfaces on arbitrary meshes. J Comp Phys 153: 26–50
Veron F, Saxena G, Misra SK (2007) Measurements of the viscous tangential stress in the airflow above wind waves. Geophys Res Lett 34:L19603. doi:10.1029/2007GL031242
Wen X (2012) The Analytical Expression for the Mass Flux in the Wet/Dry Areas Method. ISRN Applied Mathematics. 2012: Article ID 451693, 15 pp, doi:10.5402/2012/451693
Wen X (2013) Wet/dry areas method for interfacial (free surface) flows. Int J Numer Methods Fluids 71(3): 316–338
Yang D, Shen L (2010) A numerical study on the evolution and structure of a stress-driven free-surface turbulent shear flow direct-simulation-based study of turbulent flow over various waving boundaries. J Fluid Mech 650:131–180
Yang D, Shen L (2011) Simulation of viscous flows with undulatory boundaries: part II. Coupling with other solvers for two-fluid computation. J Comp Phys 230:5510–5531